ECS Journal of Solid State Science and Technology, **5** (2) P6-P11 (2016)
2162-8769/2016/5(2)/P6/6/$33.00 © The Electrochemical Society

Infiltration of ZnO in Mesoporous Silicon by Isothermal Zn Annealing and Oxidation

C. de Melo,[a,z] G. Santana,[b] V. Torres-Costa,[c,d] M. Behar,[e] J. Ferraz Dias,[e] J. L. Colaux,[f] G. Contreras-Puente,[g] and O. de Melo[a]

[a]*Physics Faculty, University of Havana, Colina Universitaria, 10400 La Habana, Cuba*
[b]*Instituto de Investigación en Materiales, Universidad Nacional Autónoma de México, Cd. Universitaria, A.P. 70-360, Coyoacán 04510, México*
[c]*Applied Physics Department, Faculty of Sciences, Universidad Autónoma de Madrid, Cantoblanco 28049, Madrid*
[d]*Centro de Micro-Análisis de Materiales, Universidad Autónoma de Madrid, Cantoblanco 28049, Madrid*
[e]*Ion Implantation Laboratory, Institute of Physics, Federal University of Rio Grande do Sul, CP 15051, CEP 91501-970, Porto Alegre, RS, Brazil*
[f]*University of Surrey Ion Beam Centre, Guildford GU2 7XH, United Kingdom*
[g]*Escuela Superior de Física y Matemáticas, Instituto Politécnico Nacional, Unidad Profesional "ALM", México D.F. 07738, México*

In this work a two-step procedure is reported for the formation of ZnO/porous silicon (PS) composites in which ZnO is embedded in the pores of sponge like mesoporous silicon. The procedure consists of an isothermal annealing of the PS layer in Zn vapors using a close space configuration and a subsequent oxidation of the Zn infiltrated in the pores. The oxidation agent and the annealing duration are optimized for a complete oxidation of the infiltrated Zn. Structure, morphology and composition of the samples were characterized by X-ray diffraction (XRD), extended X-ray absorption fine structure (EXAFS), Scanning Electron Microscopy (SEM), Energy Dispersive Spectroscopy (EDS), Rutherford backscattering spectrometry (RBS) and photoluminescence (PL). The ZnO/PS composite was observed to exhibit a broad luminescent band covering almost all the visible range.
© 2015 The Electrochemical Society. [DOI: 10.1149/2.0031602jss] All rights reserved.

Manuscript submitted July 21, 2015; revised manuscript received October 22, 2015. Published November 4, 2015.

Porous silicon (PS) has received a lot of interest after the discovery by L. T. Canham[1] of its efficient luminescence at room temperature, which makes PS a promising material in the field of optoelectronics. Furthermore, the nanometric size of the pores allows its use as template for fabrication of nanostructures.[2–5] On the other hand, the internal surface of PS can be as high as 1000 m^2/cm^3 and its refractive index can be tuned depending upon its porosity and the embedded material. All of these properties make the PS promising in sensor technology.[6–8]

Infiltration of ZnO into PS is primarily motivated by potential applications of ZnO in the field of optoelectronics, due to its wide bandgap of 3.37 eV at 300 K. The efficient luminescence and functionality of ZnO nanostructures make them useful in several applications such as UV luminescence devices,[9] piezoelectric devices,[10] ZnO - based transparent thin-film transistors,[11] chemical sensors,[12,13] photovoltaic devices[14] and solid state lighting technology.[15] Usually, white emission is obtained by combining LEDs emitting in the blue, green and red region of the electromagnetic spectrum. However, a broad band in the entire visible range, due to the coupling between UV and yellow-green emission of ZnO with the red one of PS, has been observed in ZnO/PS structures.[16,17]

ZnO has been grown on top of PS using sol-gel,[3] electrochemical deposition,[18] pulsed laser deposition,[17] spray pyrolysis[19] and sputtering.[20,21] However, up to the best knowledge of the authors, ZnO infiltration inside the pores has been demonstrated only by using a combination of sol-gel deposition and annealing.[22] In fact, special provisions have to be taken for the infiltration of mesoporous materials because pores entrance obstruction can prevent the completion of process. In the case of sponge-like mesoporous silicon, infiltration becomes particularly difficult due to the irregular and intricate arrangement of the pores. In this paper, we propose a two-step procedure consisting of using isothermal close space sublimation (ICSS)[23] for the Zn infiltration and then vapor transport of water for its subsequent oxidation. The advantage of this method is that the experimental setup is simple, inexpensive and does not require toxic precursors like other techniques.[18,24]

[z]E-mail: claudiadem@gmail.com

Experimental

PS layers were prepared by electrochemical etching of monocrystalline p^+ (100) silicon wafers (resistivity of 0.05–0.1 Ωcm). Details of the preparation of PS can be found elsewhere.[2,25] The applied current density and the anodization time were 150 mA/cm^2 and 20 s respectively. Under these conditions, a homogeneous sponge-like mesoporous silicon sample is obtained with pores diameter of a few nanometers.[25,26] To study the influence of the oxidation of PS prior to the growth experiments, some samples were subjected to a chemical etching in a H_2O:HF (5:1) solution for 10 s.

The ZnO/PS composite was prepared following the two-step process mentioned above. First, PS films were exposed to Zn vapors by placing small pieces of Zn (99.99%, provided by GOODFELLOWS) into a circular hole of a graphite crucible that was covered with the PS sample. This kind of isothermal annealing, for which PS is at the same temperature than the Zn source, prevents for uncontrolled and rapid deposition of Zn into the PS surface. In fact, in this regime, a very thin Zn layer is adsorbed in the exposed (outer and/or inner) PS surfaces promoting the Zn infiltration. In contrast, a regime with a large disequilibrium between source and substrate (i.e. a large temperature gradient as in thermal evaporation for example) would cause the obstruction of the pores entrance and the growth of a Zn film on top (and not inside) of PS. Even though the amount of Zn per unit area is very low due to the equilibrium conditions of the Zn annealing, this is compensated by the large specific area of PS leading to an appreciable amount of embedded Zn as will be discussed below. The preparation conditions are shown in Table I. All samples were annealed at 400°C, samples A and B for 15 min and samples C and D for 30 min. For the second step, the infiltrated Zn was oxidized by annealing the Zn/PS samples in water vapor during 30 or 60 min depending of the sample. In this step H_2 or He were used as carrier gases by bubbling them in distilled water. In all cases the sample temperature was 400°C.

Rutherford backscattering spectrometry (RBS) analyses were performed at the 3 MV Tandetron accelerator facility of the Ion Implantation Laboratory of the Physics Institute (Federal University of Rio Grande do Sul). For these measurements, a 3035 keV α-particle beam was employed in order to increase the sensitivity to oxygen. The energy resolution of the Si detectors was 12 keV. The spectra were simulated using the SIMNRA program[27] to determine the elemental depth profile. For one of the samples, RBS measurements were carried

Downloaded on 2017-05-23 to IP 132.248.12.211 address. Redistribution subject to ECS terms of use (see ecsdl.org/site/terms_use) unless CC License in place (see abstract).

Table I. Preparation conditions for samples studied in this work; namely, Zn isothermal annealing time (t_{Zn}), oxidation agent, oxidation annealing time (t_{ox}) and substrate etch. The crystallite size, as calculated using the Scherrer equation, is also shown. Zn isothermal and oxidation annealing processes were carried out at 400°C for all samples.

Sample	t_{Zn} (min)	Oxidation agent	t_{ox} (min)	Substrate etch	Crystallite size (nm)
A	15	$H_2 + H_20$	30	No	10
B	15	$H_2 + H_20$	30	Yes	24
C	30	$He + H_20$	30	No	11
D	30	$He + H_20$	60	Yes	18

out at the Surrey 2 MV tandem accelerator. These measurements were also performed around the ^{16}O (α, α) ^{16}O resonance at 3038 keV.[28] In this case the spectra were fitted using the DataFurnace code[29] to obtain the depth composition of the sample.

X-ray diffraction (XRD) patterns in Bragg Brentano configuration were taken using a Siemens D-5000 powder diffractometer with wavelength (λ) corresponding to Cu $K_{\alpha 1}$ radiation. Extended X-ray absorption fine structure spectroscopy (EXAFS) was performed at the SpLine in the European Synchrotron Radiation Facility at Grenoble, France. The calibration of the photon energy was performed on the Zn absorption K-edge spectrum with a reference sample of pure Zn (measured under the same conditions of the sample studied in this paper). The processing of the experimental data was performed using the Athena program, which allows energy correction, background subtraction and normalization of the data to give the EXAFS signal $\chi(k)$. Micrographs and energy dispersive spectroscopy (EDS) were performed in a Quanta 3D FEG-FEI JSM 7800-JEOL scanning electron microscopy (SEM).

Photoluminescence (PL) measurements were carried out using the 325 nm wavelength He–Cd laser line (maximum output power of 16 mW), as excitation source. The sample emission was focused into an Acton SpectraPro 2500i spectrograph and detected by a photomultiplier tube. All the spectra were corrected taking into account the spectral response of the system.

Results and Discussion

Figure 1 shows the X-ray diffraction patterns of the studied samples. The X-ray patterns show diffraction peaks that correspond to ZnO hexagonal crystalline phase (wurtzite), confirming the presence of ZnO in all the samples. XRD patterns of samples A and B additionally show two peaks at 38.8 and 43.4° indexed as (100) and (111) crystalline planes of hexagonal Zn. The peak observed at around 55° can be assigned to the reflection of the (311) crystallographic plane of Si.

In order to estimate the crystallite size of the ZnO nanocrystals, Lorentzian shapes were fitted to the most intense diffraction peaks of the patterns corresponding to the crystallographic planes with Miller indexes (100), (002) and (101). With the parameters obtained from the fitting (Bragg angle, θ; area, A and peak intensity, H) one can determine the crystallite size by using the Scherrer equation:

$$t_c = \frac{\lambda}{\beta * cos\,(\theta)}$$

Where $\lambda = 1.54$ Å is the wavelength of the K_α emission line of Cu, and $\beta = A/H$ is the integral width.

Crystallite sizes of 10 and 24 nm were calculated for samples A and B, respectively. Both samples were prepared following the same procedure except that sample B was subjected to a chemical etching before the infiltration of Zn. It is known that after porous silicon formation the inner surface is rapidly oxidized. The formation of SiO_2 consumes part of the silicon and adds oxygen to the lattice. Considering the molar mass of Si and SiO_2 (28.086 and 60.08 g/mole) and their densities (2.32 and 2.196 g/cm^3) it can be realized that when a layer of Si is transformed to SiO_2, the resulting thickness of the SiO_2 is 2.27 times larger than the thickness of unoxidized silicon layer. Then, the volume of solid material increases as a consequence of oxidation and void volume (porosity) consequently decreases. In the case of the sample etched before the ZnO infiltration the etching removed part of the oxide and increased the porosity. Therefore, we assume that the larger crystallite size in sample B is a consequence of the increased pores size in etched samples.[2,30] The crystallite size for samples C (un-etched) and D (etched) was estimated at 11 nm and 18 nm respectively, which confirms the above assumption.

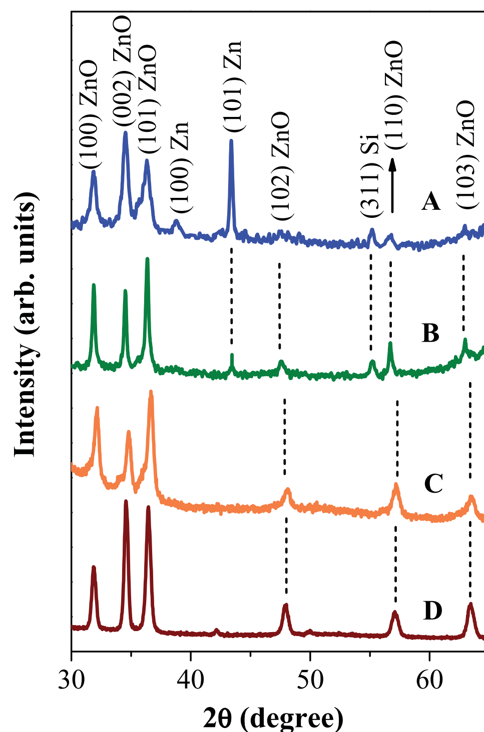

Figure 1. XRD patterns of samples A, B, C, and D in the Bragg Brentano configuration. Samples A and B were oxidized using H_2 as transport gas and samples C and D using He as transport gas. The samples B and D were etched before the Zn infiltration.

The existence of peaks associated to Zn (around 39 and 44°) in the samples oxidized using H_2 as transport gas (A and B) indicates that the oxidation was hindered in these cases. Since in samples C and D, for which He was used as carrier gas, only peaks associated to ZnO do appear, it is assumed that H_2 had an adverse effect in the oxidation process. Probably, there is an opposite behavior of H_2 and H_2O with relation of the oxidation of Zn: while H_2O tends to oxidize, H_2 tends to react with ZnO, forming water and Zn. Then, the presence of H_2 decreases the oxidation rate. This assumption is supported by the fact that H_2 is a product of the oxidation reaction: Zn (s) + H_2O (g) → ZnO (s) + H_2 (g). Then, introducing H_2 as carrier gas will increase the H_2 vapor pressure and shift the reaction equilibrium toward the reactants, decreasing the efficiency of the oxidation.

Fig. 2 shows the Fourier transforms of the k^2-weighted EXAFS functions recorded at the Zn K-edge on the samples A, B (which were observed to be only partially oxidized) and also a reference sample presented for comparison. The first and second major peaks in the radial distribution function (RDF) of the sample A and B, correspond to the nearest O and Zn atoms from the central Zn atom. As one can see, the RDF of samples A and B are in good agreement with the RDF of the reference sample except for a small peak centered at 2.67 Å. This peak can be associated with the presence of Zn (hexagonal crystal structure) in the sample since the nearest Zn atoms are at 2.665 Å[31]

Downloaded on 2017-05-23 to IP 132.248.12.211 address. Redistribution subject to ECS terms of use (see ecsdl.org/site/terms_use) unless CC License in place (see abstract).

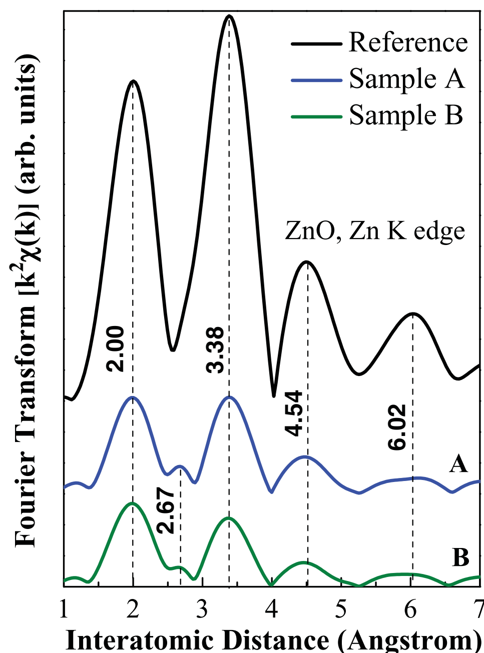

Figure 2. Fourier transforms of the k2-weighted EXAFS functions recorded at the Zn K-edge of sample A, sample B, and a reference sample of ZnO. Dashed lines are eye guides to indicate the center of the peaks.

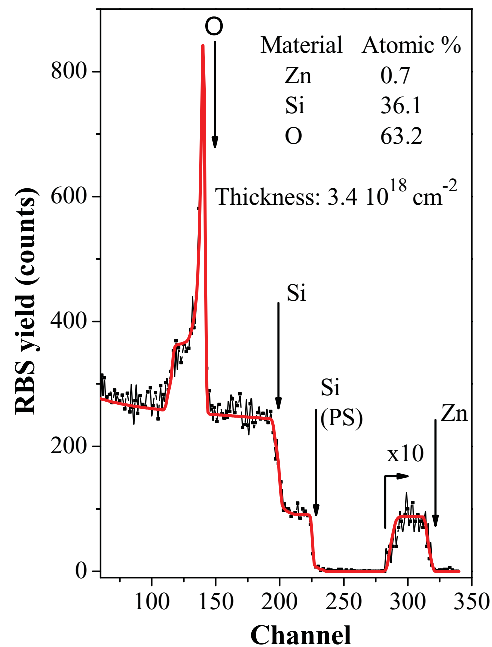

Figure 3. Rutherford backscattering spectrum (dot black curves) and simulation by SIMNRA software (solid curve) of sample C (un-etched). In the inset are presented the molar fraction of the different compound and the thickness of the sample. The first plateau associated to Zn have been multiplied by 10.

from the central Zn atom. This result is in agreement with the XRD pattern where the two peaks observed at 38.8° and 43.4° indicate the presence of non-oxidized Zn in the sample. Both XRD and RDF also highlight that the peaks ascribed to non-oxidized Zn are more intense for sample A than for sample B. It is not clear the reason of this behavior but it could be explained by the fact that in the etched sample (B), as was noted above, the pores are larger and H_2O can diffuse more easily inside the PS matrix; consequently a more efficient oxidation takes place.

RBS measurements were carried out for samples C and D in which complete Zn oxidation was verified. In Fig. 3 the RBS spectra of sample C is shown. The fact that both Zn and Si signals start at their border energy edge (i.e. incident beam energy times the kinematical factor of each element) indicates that the Zn is embedded within the PS layer rather than deposited on its surface. Moreover, Zn small intensity reflects the fact that the amount of infiltrated Zn is very small. This feature is expected as a consequence of the infiltration procedure used in this work: the source and the substrate are at the same temperature and only a few monolayers are expected to be absorbed by the internal pores walls.

The spectrum was fitted assuming a uniform distribution of O and Zn through a PS layer. The atomic percent of Zn, Si and O were 0.7%, 36.1% and 63.2% respectively. It is worth noting that due to the small amount of Zn, the statistics of the Zn portion of the spectra is poor and as a result the calculated amount of Zn has to be considered as an estimative value with a relative uncertainty probably higher than 10%. Assuming that the layer is actually made of a mixture of Si, SiO_2 and ZnO formula units (FUNs) the corresponding percent values were found to be 13.2%, 84.9% and 1.9%, respectively.

The presence of Zn in the PS matrix was also verified by SEM and EDS measurements. Fig. 4 shows a top view image of sample C. Some of the pores emerging at the surface are clearly observed which proves that the pores entrance was not completely obstructed by the ZnO infiltration. On the other hand, the presence of Zn is verified by the EDS spectrum in the inset of the figure. The average atomic percent values of Zn, Si and O were around 0.8, 40.5 and 58.7%, respectively, in relatively good agreement with RBS results. A cross sectional image in a cleaved sample is shown in Fig. 5 together with the EDS compositional profile. It can be observed that a small amount of Zn is distributed along the whole thickness of the PS layer and, similar to RBS results, the concentration of Zn is almost constants across the layer. The thickness of this PS layer was around 1.02 μm.

The thickness of the sample (d) can be also evaluated through the RBS spectra using:

$$d = \frac{\Delta}{\bar{\rho}_{at}} \qquad [1]$$

Where Δ is the areal density (proportional to the thickness), and $\bar{\rho}_{at}$ is the average atomic density of the film. Considering a compact layer,

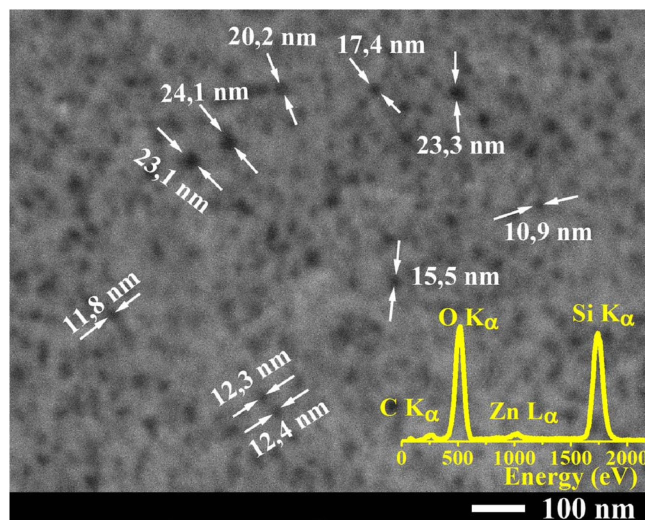

Figure 4. Top view SEM image for sample C. The sizes of some of the pores that emerge at the surface are highlighted. The EDS spectrum of the sample taken in this configuration is shown in the inset.

Downloaded on 2017-05-23 to IP 132.248.12.211 address. Redistribution subject to ECS terms of use (see ecsdl.org/site/terms_use) unless CC License in place (see abstract).

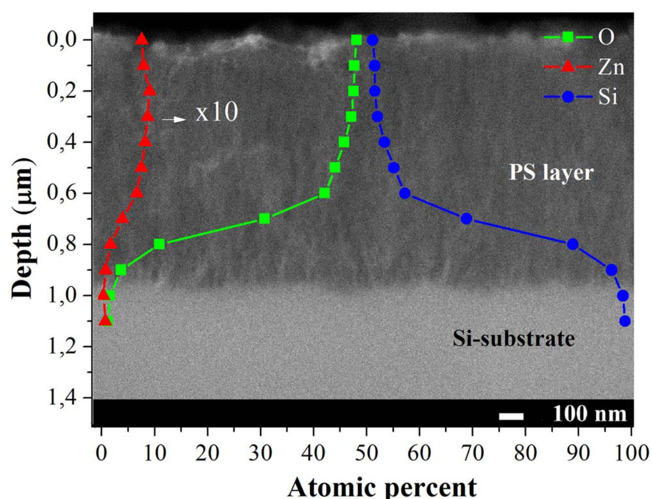

Figure 5. SEM cross sectional image of cleaved sample C. The EDS compositional profile of Zn (triangles), Si (circles) and O (squares) is overlaid.

the average FUN density ($\bar{\rho}$) is:

$$\bar{\rho} = \frac{1}{\frac{Y_{ZnO}}{\rho_{ZnO}} + \frac{Y_{SiO_2}}{\rho_{SiO_2}} + \frac{Y_{Si}}{\rho_{Si}}} \quad [2]$$

Here Y_{ZnO}, Y_{Si}, Y_{SiO_2}, ρ_{ZnO}, ρ_{Si}, ρ_{SiO_2} are the FUN fractions and FUN densities of ZnO, Si and SiO_2, respectively.

The relation between $\bar{\rho}_{at}$ and $\bar{\rho}$ is given by:

$$\bar{\rho}_{at} = \frac{\bar{\rho}}{(X_{Zn} + X_{Si})} \quad [3]$$

Where X_{Zn} and X_{Si} are the atomic fractions of Zn and Si, respectively. A detailed deduction of Eqs. 2–4 is presented in the Appendix.

Using Eqs. 1–3 a thickness of 523 nm was obtained for sample C, much smaller than the one observed in the SEM image. This is because, in determining the thickness using Eqs. 1 and 2, a compact sample was considered without taking into account the existence of a remaining porosity after the infiltration. Then, we can estimate the porosity (p) of PS after infiltration of ZnO considering that the total volume of the sample is occupied by the ZnO, SiO_2 and Si compounds plus a void volume. The thickness is expressed as in eq. 1 but the average FUN density is given now by:

$$\bar{\rho} = \frac{1 - p}{\frac{Y_{ZnO}}{\rho_{ZnO}} + \frac{Y_{SiO_2}}{\rho_{SiO_2}} + \frac{Y_{Si}}{\rho_{Si}}} \quad [4]$$

Using Eqs. 1, 3 and 4 we obtain a porosity of 49% for sample C after the ZnO infiltration, while a value of 72% was calculated[32] for the virgin PS. The fact that certain porosity remains after infiltration is in agreement with the used procedure for the infiltration.

Similar RBS spectrum (not shown here) was acquired for sample D (etched). The obtained atomic percent of Zn, Si and O were 0.2%, 56.4% and 43.4% respectively and the corresponding FUN percent of Si, SiO_2 and ZnO were found to be 61.4%, 38.2% and 0.4% respectively. In this case a thickness of 397 nm was obtained. Following the same analysis as for sample C, we obtain a porosity of 61% for sample D. Both, the Zn atomic percent and the ZnO molar percent values are smaller of that obtained for the un-etched sample C, and the remaining porosity is also higher in this case. It is not clear the reason of this difference in Zn composition between these two samples. We speculate that in larger pores as those of sample D, Zn desorption is favored during H_2O annealing and part of the Zn is re-sublimated, but more specific experiments would be necessary to obtain a real dependence between the amount of Zn and the porosity of the PS. RBS results are summarized in Table II.

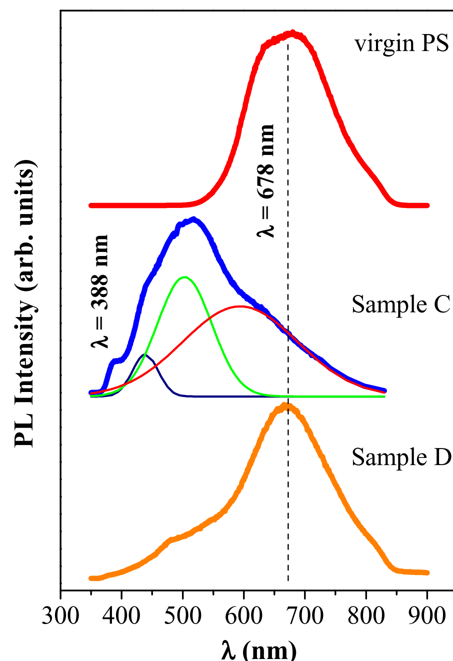

Figure 6. Photoluminescence spectra of samples C, D, and a virgin PS sample. In the case of sample C, the three Gaussian components of the spectra are shown.

Fig. 6 shows the photoluminescence spectra of a virgin PS sample together with the spectra of samples C and D. As can be seen, the virgin PS shows its typical red emission. This red luminescence is related to quantum confinement of silicon nanocrystals or, for nanocrystals of sizes below 3 nm, with transition of carriers trapped in localized gap states associated with the presence of oxygen.[33] After the infiltration of ZnO into PS, for sample C we obtain an intense white emission centered at 518 nm approximately that can be observed at naked eye when the sample is illuminated with the HeCd laser. Also a shoulder appears near 388 nm that can be attributed to the near band edge emission of ZnO.[34] The wide band centered at 518 nm can be deconvoluted into three sub-bands: a blue, a green and a red one. The blue band around 441 nm has been ascribed to transitions from a shallow donor associated with interstitial Zn in ZnO.[35,36] The green band is centered at 504 nm and has been attributed to the deep level emission originated from the single ionized oxygen vacancy.[11] On the other hand, we think that the red band, centered at 610 nm, is

Table II. Summary of the RBS measurements. The average FUN density of the layer is determined considering the densities of the components: ZnO (4.15 x 10^{22} cm^{-3}), SiO_2 (2.19 x 10^{22} cm^{-3}) and Si (4.99 x 10^{22} cm^{-3}). Knowing the actual thickness of the PS layer (measured by SEM), the porosity of the film was derived. (TFU stands for thin film units: 10^{15} at/cm^2).

Sample	Atomic fraction (%)			FUN molar fraction (%)			Average FUN density	Areal density	Derived
	Si	O	Zn	ZnO	SiO_2	Si	(FUN/cm^3)	(TFU)	porosity (%)
C	36.1	63.2	0.7	1.9	84.9	13.2	$2.4*10^{22}$	3400	49
D	56.4	43.4	0.2	0.4	38.2	61.4	$3.5*10^{22}$	2350	61

Downloaded on 2017-05-23 to IP 132.248.12.211 address. Redistribution subject to ECS terms of use (see ecsdl.org/site/terms_use) unless CC License in place (see abstract).

due to the PS substrate. This red band is blue shifted compared to the one of the pristine PS substrate probably due the surface passivation of PS by the infiltration of ZnO. As we noted before, one possible explanation of the red emission of PS is the transition of carriers in oxygen-related localized gap states. The infiltration of ZnO inside PS could passivate the surface and remove this localized states recovering the own emission of the silicon nanocrystals. In the spectrum of sample D again a broad emission in the visible range can be seen, but in this case we observe that PS emission prevails over the ZnO luminescence, since the spectrum has the most intense emission around 678 nm as in virgin PS and the blue-green emission (originated from ZnO) is considerable smaller than the observed in sample C. This can be explained because in the case of sample D a smaller amount of ZnO is formed, as concluded from RBS measurements, and therefore the contribution of ZnO to the PL is smaller than the contribution of PS.

Conclusions

It was proposed a simple and novel procedure for preparing ZnO/PS composites with ZnO infiltrated inside the pores of sponge-like mesoporous silicon. The composite is formed by a Zn isothermal annealing of the PS films in a closed space configuration followed by humid He or H_2 annealing. In the first process the internal surface of the pores is covered with Zn while in the second one, the embedded Zn is oxidized. The formation of ZnO embedded in the PS substrate was demonstrated by XRD, RBS, EDS, EXAFS and PL complementary techniques. Through XRD and EXAFS measurements we conclude that He is a more efficient carrier gas than H_2 which can be explained by thermodynamic considerations regarding the oxidation reaction. In addition, it was also shown that in samples etched with H_2O:HF (5:1) before the infiltration, ZnO crystallites are larger due to the increased pores size in etched PS. RBS and EDS experiments show that Zn infiltration in PS is nearly uniform in composition and the composition and porosity for the composites was estimated. ZnO embedded samples display an intense wide luminescence band ranging from the ultraviolet to the red extreme of the visible region composed by the luminescence of ZnO and that of the passivized PS. The shape of this wide luminescence band can be modified by controlling the amount of embedded ZnO.

Acknowledgments

This work was partially supported by the SECITI-CLAF program, the CAPES-MES CUBA project 121/11 and the agreement between the University of Havana and the Universidad Autónoma de Madrid. The authors thank S. de Roux for technical assistance, Darío Gallach and the SpLine staff for their help in the realization of the EXAFS measurements.

Appendix

Fitting the RBS spectrum allows one to determine the atomic concentration of the different elements present in the sample (X_{Zn}, X_{Si} and X_O) as well as the magnitude Δ, the areal density of the sample (proportional to the thickness). In order to obtain the thickness (d) we use the following expression:

$$d = \frac{\Delta}{\bar{\rho}_{at}} \quad [A1]$$

Where $\bar{\rho}_{at}$ is the average atomic density, which can be calculated considering all the elements present in the sample.

It can be assumed that inside PS there is a mixture of Si, SiO_2 and ZnO formula units (FUNs) and that all oxygen atoms are bonded to Si or Zn forming the SiO_2 and ZnO compounds, respectively. Then we consider FUN fractions and FUN densities of each compound instead of atomic fractions and atomic densities of the different elements.

To obtain the average FUN density (calculated considering all the compounds present in the sample) we consider that the total volume of the sample is occupied by ZnO, SiO_2 and Si compounds in the case of a compact sample without porosity (Eq. A2, or adding a void volume for a porous sample (Eq. A3).

$$V_T = V_{ZnO} + V_{SiO_2} + V_{Si} \quad [A2]$$

$$V_T = V_{ZnO} + V_{SiO_2} + V_{Si} + pV_T \quad [A3]$$

In Eq. A3 p is the porosity of the sample.

The volume occupied by each material can be calculated as the number of FUNs of each compound divided by their FUN density (ρ_{ZnO}, ρ_{SiO_2}, ρ_{Si}). Considering that the number of FUNs of each compound is the FUN fraction (Y_{ZnO}, Y_{SiO_2}, Y_{Si}) times the total amount of FUNs (N), we can express the total volume as in Eq. A4 for a compact sample or as in Eq. A5 for a porous one:

$$V_T = \left(\frac{Y_{ZnO}}{\rho_{ZnO}} + \frac{Y_{SiO_2}}{\rho_{SiO_2}} + \frac{Y_{Si}}{\rho_{Si}}\right) N \quad [A4]$$

$$V_T = \left(\frac{Y_{ZnO}}{\rho_{ZnO}} + \frac{Y_{SiO_2}}{\rho_{SiO_2}} + \frac{Y_{Si}}{\rho_{Si}}\right) N + pV_T \quad [A5]$$

Since the average FUN density $\bar{\rho}$ is equal to N/V_T we obtain the following expression for a compact (Eq. A6) and a porous sample (Eq. A7):

$$\bar{\rho} = \frac{1}{\left(\frac{Y_{ZnO}}{\rho_{ZnO}} + \frac{Y_{SiO_2}}{\rho_{SiO_2}} + \frac{Y_{Si}}{\rho_{Si}}\right)} \quad [A6]$$

$$\bar{\rho} = \frac{1-p}{\left(\frac{Y_{ZnO}}{\rho_{ZnO}} + \frac{Y_{SiO_2}}{\rho_{SiO_2}} + \frac{Y_{Si}}{\rho_{Si}}\right)} \quad [A7]$$

Now we need to determine the relation between $\bar{\rho}_{at}$ and $\bar{\rho}$. In order to do that we will find the relation of the FUN fractions of ZnO, SiO_2 and Si (Y_{ZnO}, Y_{SiO_2} and Y_{Si}) with the atomic fractions of Zn, Si and O (X_{Zn}, X_{Si}, X_O) respectively. The number of ZnO FUNs will be equal to the number of Zn atoms on the assumption that all Zn atoms are bonded to O atoms to form ZnO FUNs. Similarly, we can write the following equations for each compound:

$$Y_{ZnO} = \frac{N_{Zn}}{N} = \frac{X_{Zn}}{N} N_a \quad [A8]$$

$$Y_{SiO_2} = \frac{(N_O - N_{Zn})/2}{N} = \frac{X_O - X_{Zn}}{2N} N_a \quad [A9]$$

$$Y_{Si} = \frac{N_{Si} - \left(\frac{N_O - N_{Zn}}{2}\right)}{N} = \frac{X_{Si} - \left(\frac{X_O - X_{Zn}}{2}\right)}{N} N_a \quad [A10]$$

But we know that $Y_{ZnO} + Y_{SiO_2} + Y_{Si} = 1$. Therefore:

$$N = (X_{zn} + X_{Si}) N_a \quad [A11]$$

Substituting Eq. A11 in Eqs. A8–A10 the FUNs fractions can be expressed as:

$$Y_{ZnO} = \frac{X_{Zn}}{(X_{zn} + X_{Si})};\ Y_{SiO_2} = \frac{X_O - X_{Zn}}{2\ (X_{zn} + X_{Si})};\ Y_{Si} = \frac{X_{Si} - \left(\frac{X_O - X_{Zn}}{2}\right)}{(X_{zn} + X_{Si})}$$

Finally, as the average atomic density is equal to N_a/V, using Eq. A11 we can find the relation between $\bar{\rho}_{at}$ and $\bar{\rho}$:

$$\bar{\rho}_{at} = \frac{\bar{\rho}}{(X_{zn} + X_{Si})}$$

References

1. L. T. Canham, *Appl. Phys. Lett.*, **57**, 1046 (1990).
2. C. de Melo, S. Larramendi, V. Torres-Costa, J. Santoyo-Salazar, M. Behar, J. Ferraz-Dias, and O. de Melo, *Micropor. Mesopor. Mater.*, **188**, 93 (2014).
3. R. G. Singh, F. Singh, D. Kanjilal, V. Agarwal, and R. M. Mehra, *J. Phys. D: Appl. Phys.*, **42**, 062002 (2009).
4. O. de Melo, C. de Melo, G. Santana, J. Santoyo, O. Zelaya-Angel, J. G. Mendoza-Álvarez, and V. Torres-Costa, *Appl. Phys. Lett.*, **100**, 263110 (2012).
5. A. I. Belogorokhov, L. I. Belogorokhova, A. Pérez-Rodríguez, and S. Gavrilov, *Appl. Phys. Lett.*, **73**, 2768 (1998).
6. H. Ouyang, C. C. Striemer, and P. M. Fauchet, *Appl. Phys. Lett.*, **88**, 163108 (2006).
7. V. A. Moshnikov, I. Gracheva, A. S. Lenshin, Y. M. Spivak, M. G. Anchkov, V. V. Kuznetsov, and J. M. Olchowik, *J. Non-Cryst. Solids*, **358**, 590 (2012).
8. Y. Cui, Q. Wei, H. Park, and C. M. Lieber, *Science* **293**, 1289 (2001).
9. J.-H. Lim, C.-K. Kang, K.-K. Kim, I.-K. Park, D.-K. Hwang, and S.-J. Park, *Adv. Mater.*, **18**, 2720 (2006).
10. Y. Lu, N. W. Emanetoglu, and Y. Chen, in Zinc Oxide Bulk, Thin Films and Nanostructures, processing, properties and applications, C. Jagadish and S. Pearton, Editors, p. 443, Elsevier Ltd. (2006).

Downloaded on 2017-05-23 to IP 132.248.12.211 address. Redistribution subject to ECS terms of use (see ecsdl.org/site/terms_use) unless CC License in place (see abstract).

11. Ü. Özgür, Ya. I. Alivov, C. Liu, A. Teke, M. A. Reshchikov, S. Doğan, V. Avrutin, S.-J. Cho, and H. Morkoç, *J. Appl. Phys.*, **98**, 041301 (2005).
12. V. Aroutiounian, V. Arakelyan, V. Galstyan, K. Martirosyan, and P. Soukiassian, *IEEE Sens. J.*, **9**(1), 9 (2009).
13. F. Fang, J. Futter, A. Markwitz, and J. Kennedy, *Nanotechnology*, **20**, 245502 (2009).
14. W. Zhang, Q. Meng, B. Lin, and Z. Fu, *Sol. Energy Mater. Sol. Cells*, **92**, 949 (2008).
15. Vinod Kumar, S. Som, Vijay Kumar, Vinay Kumar, O. M. Ntwaeaborwa, E. Coetsee, and H. C. Swart, *Chem. Eng. J.*, **255**, 541 (2014).
16. E. Kayahan, *J. Lumin.*, **130**, 1295 (2010).
17. Cai-feng Wang, B. Hu, and Hou-hui Yi, *Optik*, **123**, 1040 (2012).
18. Y. L. Liu, Y. C. Liu, H. Yang, W. B. Wang, J. G. Ma, J. Y. Zhang, Y. M. Lu, D. Z. Shen, and X. W. Fan, *J. Phys. D: Appl. Phys.*, **36**, 2705 (2003).
19. H. Elhouichet and M. Oueslati, *Mater. Sci. Eng.*, **B 79**, 27 (2001).
20. K. A. Salman, K. Omar, and Z. Hassan, *Mater. Lett.*, **68**, 51 (2012).
21. Y. Kumara, J. Escorcia Garcia, F. Singh, S. F. Olive-Méndez, V. V. Sivakumar, D. Kanjilal, and V. Agarwal, *Appl. Surf. Sci.*, **258**, 2283 (2012).
22. D. Verma, A. Kharkwal, S. N. Singh, P. K. Singh, S. N. Sharma, S. S. Mehdi, and M. Husain, *Solid State Sci*., **37**, 13 (2014).
23. O. de Melo, E. Sánchez, H. Rodríguez, S. De Roux, F. Rábago-Bernal, and J. Ruiz-García, *Mater. Chem. Phys.*, **59**, 120 (1999).
24. B. H. Juárez, P. D. García, D. Golmayo, A. Blanco, and C. López, *Adv. Mater.*, **17**, 2761 (2005).
25. M. Utriainen, S. Lehto, L. Niinistö, Cs. Dücsó, N. Q. Khanh, Z. E. Horvárth, I. Bársony, and B. Pécz, *Thin Solid Films*, **297**, 39 (1997).
26. V. Torres-Costa, R. J. Martín-Palma, and J. M. Martínez-Duart, *Appl. Phys. A*, **79**, 1919 (2004).
27. M. Mayer, in *Proceedings of the 15th Internacional Conference on the Application of Accelerators in Research and Industry*, J. L. Dugan and I. L. Morgan, Editors, American Institute of Physics Conference Proceedings, **475**, 541 (1999).
28. J. L. Colaux, G. Terwagne, and C. Jeynes, *Nuclear Instruments and Methods in Physics Research Section B: Beam Interactions with Materials and Atoms*, **349**, 173 (2015).
29. N. P. Barradas, C. Jeynes, and R. P. Webb, *Appl. Phys. Lett.*, **71**, 291 (1997).
30. E. V. Astrova and V. A. Tolmachev, *Materials Science and Engineering*, **B 69-70**, 142 (2000).
31. H. E. Swanson, E. Tatge, and R. K. Fuyat, *Ann. Phys.*, **12**, 121 (1953).
32. V. Torres-Costa, F. Pászti, A. Climent-Font, R. J. Martín-Palma, and J. M. Martínez-Duart, *Journal of the Electrochemical Society*, **152**(11), G846 (2005).
33. M. V. Wolkin, J. Jorne, P. M. Fauchet, G. Allan, and C. Delerue, *Phys. Rev. Lett.*, **82**, 197 (1999).
34. S. Cho, J. Ma, Y. Kim, Y. Sun, G. K. L. Wong, and J. B. Ketterson, *Appl. Phys. Lett.*, **75**, 2761 (1999).
35. H. Zeng, W. Cai, P. Liu, X. Xu, H. Zhou, C. Klingshirn, and H. Kalt, *ACS nano*, **2**(8), 1661 (2008).
36. D. H. Zhang, Z. Y. Xue, and Q. P. Wang, *J. Phys. D: Appl. Phys.*, **35**, 2837 (2002).

Downloaded on 2017-05-23 to IP 132.248.12.211 address. Redistribution subject to ECS terms of use (see ecsdl.org/site/terms_use) unless CC License in place (see abstract).